PHYSICAL REVIEW FLUIDS **3**, 124306 (2018)

Morphodynamics of a sediment bed in a fluid-filled cylinder during spin-down: An experimental study

A. S. González-Vera, M. Duran-Matute,[*] and G. J. F. van Heijst
Fluid Dynamics Laboratory, Department of Applied Physics and J.M. Burgers Center for Fluid Dynamics, Eindhoven University of Technology, P.O. Box 513, 5600 MB Eindhoven, Netherlands

(Received 28 July 2018; published 20 December 2018)

This paper presents a detailed experimental study of the evolution of a sediment bed under the action of the boundary layers formed under a spin-down flow in a rotating fluid-filled cylindrical tank. Both complete and partial spin-down are considered, i.e., with the tank coming to a complete stop or being only partially decelerated. Two nondimensional numbers, the Reynolds (Re) and Rossby (Ro) numbers, govern the flow. During the spin-down, the bed morphology changes, exhibiting distinct characteristic patterns. The changes are measured using a light attenuation technique (LAT). Background rotation suppresses the emergence of instabilities and turbulence, making the patterns more regular and smoother. In spite of the differences and complexity in the patterns, radially inward transport is explained by the total radial force exerted by the flow as computed using classical expressions for the structure of laminar boundary layers.

DOI: 10.1103/PhysRevFluids.3.124306

I. INTRODUCTION

For millennia, it has been observed that swirling flows can transport heavy particles, such as sediment, toward their core [1] and even lift them from the ground. In the natural world, this is the case for dust devils [2,3], rip tides [4,5], and tornadoes [6–8]. In industry, the transport of heavy particles by swirling flows toward their core is also relevant, for example, in erosion-measurement devices [9], combusters [10,11], and whirlpool vats [12].

This phenomenon is reminiscent of the "tea leaves problem" used to explain the formation of meanders in rivers [13]. In this description, tea leaves at the bottom of a cup are collected at the center when the water is stirred because the centrifugal force is weaker at the bottom than at the surface, giving rise to the secondary circulation that is radially inward at the bottom and axially upward in the center. However, a more detailed and quantitative description of the transport of sediment under swirling flows requires delving into the characteristics of the bottom boundary layer where the flow and the sediment interact.

To obtain this description, a spin-down flow, obtained by decelerating a fluid-filled rotating cylindrical container, is ideal because the flow and the boundary layer are well controlled and well defined. (For in-depth reviews of spin-up and spin-down flows, see Refs. [14–17].) The boundary layer and the associated secondary circulation have been thoroughly described in an unbounded domain over an infinite solid disk, where the disk, the fluid, or both are rotating [18–21]. Particular cases are the von Karman flow, the Ekman-type boundary layer flow, and the Bödewadt boundary layer flow, which are quintessential examples of the boundary layers under a swirling flow. These boundary layers and intermediate cases are three-dimensional prototypical flows [22] used as models for turbomachinery [23] and geophysical swirling flows [24–27].

---

[*] m.duran.matute@tue.nl

Previous studies on the interaction between a spin-up or spin-down flow and a granular bottom inside of a cylinder [28–30] have observed the emergence of spiral patterns on the sediment bed. In particular, these studies focus on the number of ripples or spiral arms that form on the azimuthal angle of the spiral arms and on the generating mechanism. However, the parameter space explored was limited (focusing primarily on spin-up flows), and there were no measurements of the sediment volume displaced to quantify the efficiency of the flow in transporting sediment.

To address these points, we performed an experimental study in which a spin-down flow was generated over a bed of light plastic particles. The light weight of the particles allowed the exploration of a large region of the parameter space. Changes in the bed thickness were measured using a light attenuation technique based on the work by Munro and Dalziel [31]. The net volume of displaced particles is quantified by comparing the bed thickness measured at several instants across the domain with the initial bed thickness. Both complete and partial spin-down experiments were performed, i.e., with the tank coming to a complete stop or being only partially decelerated. This allows us to distinguish the effect of background rotation. For all experiments, a total radial force is calculated based on the exerted bottom shear stress obtained through the classical laminar boundary layer solutions. The net radial transport of particles is described as a function of this force.

The present paper is organized as follows. A description of the problem is given in Sec. II, and the experimental setup is described in Sec. III. Results are presented in Sec. IV, first focusing on the qualitative description of changes in the morphology, followed by the quantitative measurements of the net sediment transport. Results are discussed in Sec. V, and the conclusions are outlined in Sec. VI.

II. DESCRIPTION OF THE PROBLEM

In the initial stage of the experiment, a liquid-filled cylinder with a flat sediment bed at the bottom is rotating under solid-body rotation at a rate Ω_i. Then, its velocity is impulsively decreased to a lower value (Ω_f). What occurs to the sediment bed, how it changes, and how much sediment is transported are the interests of this study.

The decrease in rotation rate results in a difference in angular velocity ($\Delta\Omega = \Omega_i - \Omega_f$) between the bulk of the fluid and its surrounding boundaries, including the sediment bed. A boundary layer develops with a radially inward flow with the velocity magnitude proportional to $\Delta\Omega$. Because of conservation of mass, the radially inward flow is compensated by an upward flow parallel to the rotation axis. Subsequently, the relative flow slowly decays, and the fluid adjusts slowly until it reaches the new angular velocity of the container in a process commonly referred to as "spin-down".

The hydrodynamic spin-down problem is governed by three nondimensional parameters: the Rossby number ($\mathrm{Ro} = \Delta\Omega/\Omega_f$), which represents the ratio between the inertial forces and the Coriolis force; the Reynolds number ($\mathrm{Re} = \Delta\Omega R^2/\nu$, where R is the radius of the domain and ν is the kinematic viscosity of the fluid), which represents the ratio between the inertial forces and the viscous forces; and the aspect ratio ($A_r = H/R$, where H is the fluid height). The fluid height and the radius of the tank remain unchanged so A_r is kept constant with a value close to 1. For this value of A_r, the flow is governed by the effects of the boundary layer at the bottom [14].

For extreme Ro values, two well-known cases of the spin-down flow can be identified [15]: the Bödewadt flow ($\mathrm{Ro} = \infty$), where a fluid rotates over a solid nonrotating boundary, and the Ekman-type flow ($\mathrm{Ro} \ll 1$), where the boundary and the fluid are corotating with a small angular velocity difference. The boundary layer for both of these cases has a qualitatively similar structure with the thickness given by

$$\delta_E = \sqrt{\nu/\Omega_f}, \tag{1}$$

for the Ekman-type flow [32] and by

$$\delta_B = \sqrt{\nu/(\Delta\Omega)}, \tag{2}$$

for the Bödewadt flow [19].

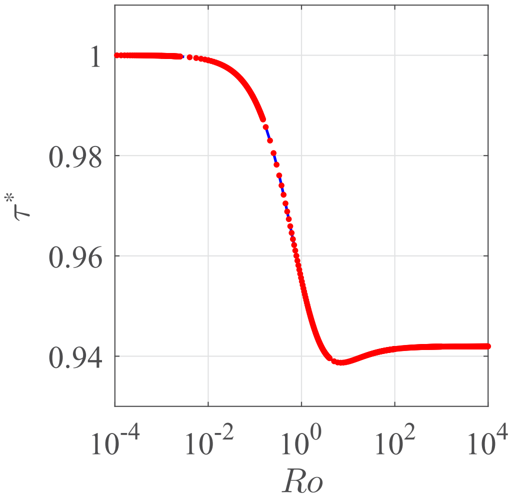

FIG. 1. Value of τ^* in the bottom boundary layer obtained numerically as a function of Ro.

Although part of the experiments do not fit either of these two characteristic cases due their intermediate Ro value (categorized as BEK flows by Lingwood [33] from the initials of Bödewadt, Ekman and von Kármán), the behavior of the flow is still qualitatively similar so that the boundary layer thickness can be redefined as

$$\delta = \sqrt{\frac{\nu}{\Delta\Omega + \Omega_f}}. \tag{3}$$

This definition is valid for all Ro values, including the extreme cases when $\Omega_f = 0$ (Bödewadt flow) or $\Delta\Omega \ll \Omega_f$ (Ekman-type flow). Although δ is time dependent for the Bödewadt flow, it is approximated as a constant since the typical decay time of the flow, which governs the changes in the boundary layer thickness, is much longer than the typical timescale for the changes in the bed and the duration of an experiment.

For a bed of mobile particles, particles are set into motion due to the shear stress (τ) exerted by the flow on the bed, following the common understanding of sediment motion [34]. This requires τ to exceed a critical value (τ_{cr}), which depends on the density (ρ_p), shape, and size of the particles (R_p) [35,36]. If the value of τ_{cr} is exceeded, a net displacement of particles will occur and will differ depending on the magnitude of τ. Depending the net particle displacement, changes in the bed morphology can occur.

To calculate the shear stress exerted in a solid flat bottom by a spin-down flow, we use the relation

$$\tau = \rho_f \nu \frac{\partial u_r}{\partial z} = \frac{\rho_f \nu \Delta\Omega r}{\delta} \frac{\partial {u_r}^*}{\partial z^*}, \tag{4}$$

where ρ_f is the density of the fluid and ${u_r}^*, z^*$ are the nondimensional radial velocity and vertical coordinate, respectively. To calculate the dimensionless shear stress ($\tau^* = \partial {u_r}^*/\partial z^*$) and its dependence on the value of Ro, the stationary and axisymmetric equations of a rotating flow over a flat disk are solved numerically, following the methodology used by Rogers and Lance [20] and Schlichting and Gersten [15]. As shown in Fig. 1, it is found that as extreme (both small and large) Ro values are approached (i.e., for either Ekman- or Bödewadt-type flows) τ^* remains constant, with a transition between these two values occurring around $10^{-2} \lesssim \mathrm{Ro} \lesssim 10^{2}$. This transition occurs because the thickness of the boundary layer increases for high Ro values and diminishes for low Ro values, reducing and incrementing τ respectively.

Integrating the shear stress over the domain and considering that τ does not vary with the morphology changes, the total radial force F_r is given by

$$F_r = \iint_D \tau_r dA = 2\pi\rho_f \nu \int_R \left(\frac{\Delta\Omega r}{\delta}\frac{\partial {u_r}^*}{\partial z^*}\right) r dr = \frac{2}{3}\pi\rho_f \nu R^3 \frac{\Delta\Omega}{\delta}\tau^*. \tag{5}$$

Furthermore, using the definition of δ [Eq. (3)] and substituting it in Eq. (5), we obtain

$$F_r = \frac{2}{3}\pi\rho_f \nu^2 \tau^* \mathrm{Re}^{3/2}\left(1 + \frac{1}{\mathrm{Ro}}\right)^{1/2} = \frac{2}{3}\pi\rho_f \nu^2 F^*, \tag{6}$$

where

$$F^* = \tau^* \mathrm{Re}^{3/2}\sqrt{(1 + \mathrm{Ro}^{-1})} \tag{7}$$

is the dimensionless total radial force. From this, it is understood that the force exerted by the spin-down flow increases with both the imposed velocity difference and the presence of rotation, being able to obtain the same magnitude of force with different values of Re and Ro. This is because the boundary layer thickness decreases as the Ro value is reduced, leading to a larger shear stress and thus stronger forces on the bed.

For this study, a single type of particle is used, requiring a single value of τ_{cr} to set particles into motion. Since the particle properties are kept fixed, we characterize the experiments by two nondimensional parameters: Re and Ro. For convenience, we will describe the experiments as a function of the inverse of the Rossby number Ro^{-1}, so that for experiments with $\Omega_f = 0$, $\mathrm{Ro}^{-1} = 0$. Note that the total force [Eq. (6)] increases with increasing values of both Re and Ro^{-1}.

III. EXPERIMENTAL SETUP

The experimental setup (Fig. 2) consisted of two concentric plexiglass containers, an outer square tank (with dimensions $58 \times 58 \times 53\,\mathrm{cm}^3$) and a inner cylindrical tank with a radius of $R = 24.4$ cm, which were placed on top of a computer-controlled rotating table. Both containers had an open top and were filled to a height $H = 28$ cm with a brine solution, with density $\rho_f = 1.021\,\mathrm{g\,cm}^{-3}$ and viscosity $\nu \sim 1.0 \times 10^{-6}\,\mathrm{m}^2\,\mathrm{s}^{-1}$. The outer tank was used to avoid optical deformations when viewing from the side. Below the tanks, an illumination bank composed of an array of nine fluorescent tubes was placed. A white acrylic sheet was placed between the lights and the containers as a light diffuser to increase the homogeneity in the illumination. A camera was positioned directly above the tank's center, looking vertically down. A second camera was positioned on the side of the tank, in such a way as to properly observe the complete surface of the particle bed.

Inside of the cylindrical tank, translucent, spherical polystyrene particles were added until a layer of thickness $h_p \simeq 2$ cm was formed at the bottom. The particles had a diameter $d = 583 \pm 014\,\mu$m, and a density $\rho_p = 1.05\,\mathrm{g\,cm}^{-3}$. The low density difference and small particle size were chosen so that particles would be responsive to the flow. Using the values of the particle properties and the velocity of the spin-down flow, the Stokes number is calculated, which is defined as the ratio between the characteristic time of a particle and the characteristic time of the flow:

$$\mathrm{St} = \frac{t_p}{t_f} = \frac{\rho_p d^2 \Delta\Omega}{18\nu\rho_f}. \tag{8}$$

For the experiments presented in the current paper, $0.0294 \geqslant \mathrm{St} \geqslant 0.0053$. This means that our results are limited to particles that respond quickly to changes in the flow.

Each experiment began by increasing the speed of the rotating table up to a rotation rate Ω_i (of up to $2.5\,\mathrm{rad\,s}^{-1}$). This had to be done slowly to avoid disturbing the flat particle bed. Once the system had reached an angular speed Ω_i and the fluid had achieved a solid-body rotation, the rotating table was decelerated to a lower rotation rate Ω_f to produce the spin-down flow. The deceleration rate of the rotating table was $d\Omega/dt \sim -0.2\,\mathrm{rad\,s}^{-2}$ and is restricted due to the mechanical limitations of

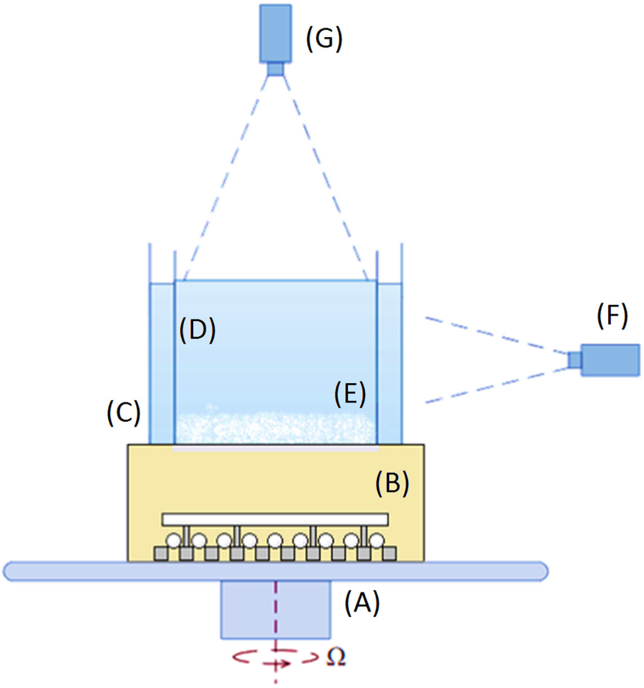

FIG. 2. Schematic of the experimental setup used, consisting of a rotating table (A), a base containing the light source (B), an outer square tank (C), an interior cylindrical tank (D), a layer of particles of height h_p (E), and side (F) and top (G) cameras.

the table. For the experiment with the largest $\Delta\Omega$ value ($\Delta\Omega = 1.5\,\mathrm{rad\,s^{-1}}$), the deceleration rate of the table had to be set to $-0.1\,\mathrm{rad\,s^{-2}}$.

Depending on the value of Ω_f, experiments are classified as partial spin-down ($\Omega_f > 0$) or as complete spin-down ($\Omega_f = 0$). The rotation and deceleration rates for the experiments were limited by the technical specifications of the rotating table. As for $\Delta\Omega$, its values were chosen based on the rotation rate difference necessary to move the particles when $\Omega_f = 0$. For the sediment used in the experiments, the minimal rotation rate difference necessary to begin moving individual particles at the surface of the particle layer was $\Delta\Omega \approx 0.2\,\mathrm{rad\,s^{-1}}$. Each experiment was recorded for a duration of 4 min. To have a well-defined initial condition for all experiments, care was taken to achieve a uniform particle bed thickness.

The values of Ω_i, Ω_f, $\Delta\Omega$, Re, and Ro for the 29 different experiments are presented in Table I.

A. Light attenuation technique (LAT)

Changes in the distribution of the particle layer thickness caused by the spin-down flow were determined by using a light attenuation technique (LAT) based on previous work by Munro and Dalziel [31]. This method requires illuminating the particle layer from below. The intensity of the light that passes through the bed decreases due to reflections, refractions, and absorptions. The recorded light intensity (I) can then be correlated to the particle bed thickness (h_p), which varies across the domain (x, y). In order to obtain measurements of the bed thickness from $I(x, y)$, an empirical relation based on the Beer-Lambert law was used:

$$h = d\left[\frac{1}{\alpha}\log\left(\frac{I}{I_0}\right)\right]^{1/p}, \tag{9}$$

TABLE I. Table with the imposed initial rotation rate (Ω_i) and final rotation rate (Ω_f) for all experiments. The $\Delta\Omega$, Re number, and Ro number for each experiment are also presented.

Ω_i (rad/s)	Ω_f (rad/s)	$\Delta\Omega$ (rad/s)	Re	Ro
0.3	0	0.3	17 900	∞
0.411	0.111	0.3	17 900	2.703
0.744	0.444	0.3	17 900	0.6757
0.9	0.6	0.3	17 900	0.5
1.2	0.9	0.3	17 900	0.3333
1.6	1.3	0.3	17 900	0.2308
1.9	1.6	0.3	17 900	0.1875
2.58	2.28	0.3	17 900	0.1316
0.4	0	0.4	23 800	∞
0.463	0.063	0.4	23 800	6.349
0.65	0.25	0.4	23 800	1.6
0.8	0.4	0.4	23 800	1.0
1.2	0.8	0.4	23 800	0.5
1.6	1.2	0.4	23 800	0.3333
1.9	1.5	0.4	23 800	0.2667
2.3	1.9	0.4	23 800	0.2105
0.5	0	0.5	29 800	∞
0.54	0.04	0.5	29 800	12.5
0.66	0.16	0.5	29 800	3.125
0.9	0.4	0.5	29 800	1.25
1.2	0.7	0.5	29 800	0.7143
1.7	1.2	0.5	29 800	0.4167
2.1	1.6	0.5	29 800	0.3125
2.46	1.96	0.5	29 800	0.2551
0.6	0	0.6	35 700	∞
0.7	0	0.7	41 700	∞
0.8	0	0.8	47 600	∞
0.9	0	0.9	53 600	∞
1.5	0	1.5	89 300	∞

where h is the reconstructed height distribution for each pixel in the domain, $I = I(x, y)$ is the light intensity measured, $I_0 = I_0(x, y)$ is the light intensity for a reference thickness (h_{ref}), d is the particle diameter, and α and p are calibration parameters. However, due to spatial inhomogeneities in the illumination, a pixelwise calibration was used. This requires rewriting Eq. (9) as

$$h_p = (A - B \log I)^C, \tag{10}$$

where A, B, and C are coefficient matrices for each pixel in the measurement area and are of equal size as I. The values of the coefficient matrices in Eq. (10) were determined by taking multiple reference measurements of I at defined thicknesses of the particle layer (measurements were made from 0 to 2 cm every 0.25 cm) and finding the best fitting curve for each pixel value. Figure 3 shows the comparison between the reconstructed thickness of the particle bed using the calculated calibration and the reference bed thickness.

Using this method to measure the bed thickness has the benefit of providing information dynamically in time, since the thickness of the bed is reconstructed from the recorded light intensity. However, since the particle bed could not be perfectly flattened (resulting in small variations in the particle bed surface), there was an error associated with the reconstruction of the particle bed. The standard deviation in the error is of approximately three times the particle size. The accuracy

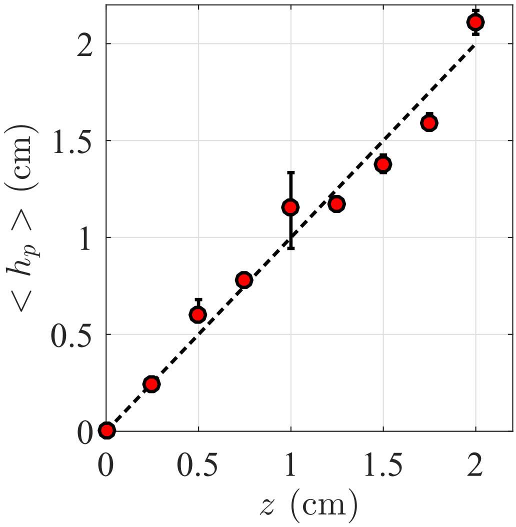

FIG. 3. Reconstructed average bed thickness (h_p) compared with the bed thickness measured at every level used for the performed calibration (z). Error bars indicate the standard deviation of the reconstruction.

of the measurement is further diminished by changes in the particle packing and the presence of suspended particles. Once particles settle and stop moving, the accuracy of the method is regained. A slight increase in error was also caused by the deformation of the water surface when $\Omega_f > 0$. While the changes in the water surface height were small (maximum difference was ±0.7 cm), this deformation produced changes in conversion between pixel and physical length, from 0.0509 to 0.0520 cm/px. However, as this is an increase of error close to 6% for the case with the highest background rotation, $\Omega_f = 2.28\,\mathrm{rad\,s^{-1}}$, it was deemed negligible. No light intensity changes were observed to occur due to the surface deformation.

IV. EXPERIMENTAL RESULTS

The radially inward secondary motion and the primary azimuthal flow exert a shear stress (τ) on the surface of the particle layer. If this stress is larger than the critical shear stress τ_{cr}, particles will move, describing spirals while traveling radially inward. Flow instabilities, particle-particle interactions, and the effect of the changing bed on the flow all contribute to a rich morphodynamical behavior of the sediment bed. One of the interesting consequences of this morphodynamical behavior is the formation of patterns on the particle bed.

A. Patterns in the particle bed

The emergence of patterns is a property observed in all the experiments performed, regardless of the net amount of sediment displaced. How patterns emerge and what their defining characteristics are depend on the values of the dimensionless parameters, Re and Ro, of the experiment. We classify the experiments into six categories depending on the pattern observed at the end.

For the smallest Re ($1 \times 10^4 \lesssim \mathrm{Re} \lesssim 3 \times 10^4$) and Ro^{-1} values, a spiral pattern emerges on the particle bed due to the inward spiralling transport of the particles. As shown Fig. 4(a), this pattern is characterized by predominant spiral ripples, secondary small radial ripples, and a circular area (with radius, r_{cr}) in the center of the tank where particles do not move. Small increases in Ro^{-1} or Re values causes more particles to be displaced, causing the spiral and radial ripples to increase in height and r_{cr} to diminish.

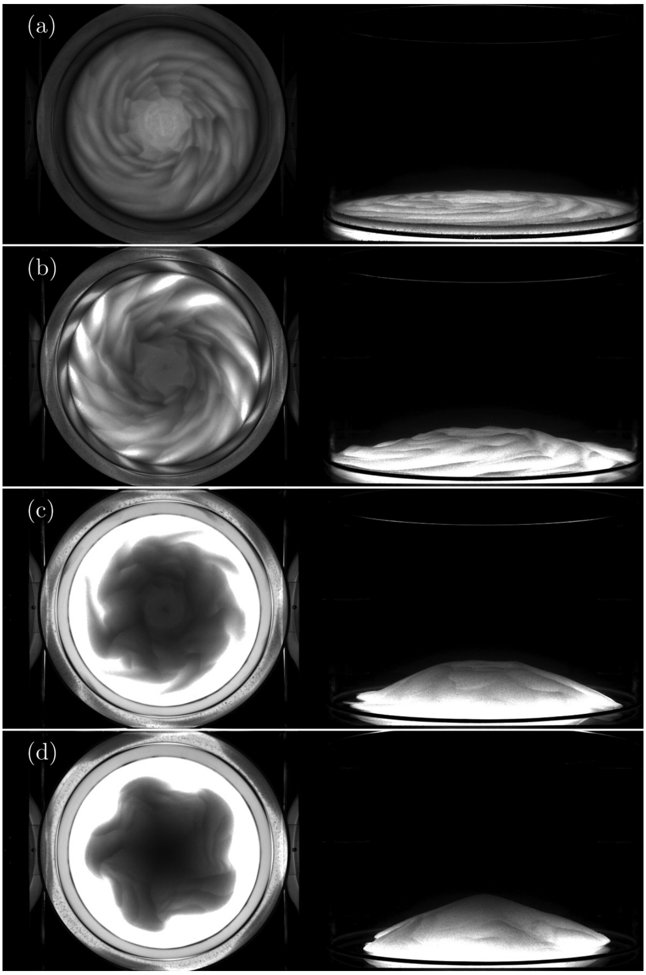

FIG. 4. Patterns formed for four experiments with $\mathrm{Ro}^{-1} = 0$ and increasing Re values. (a) Spiral pattern that emerged in the granular bed with $\mathrm{Re} = 29\,800$. (b) A complex spiral that emerged with $\mathrm{Re} = 35\,700$. (c) Semiconical dome with spiral arms that formed with $\mathrm{Re} = 41\,700$. (d) Semiconical dome that formed with $\mathrm{Re} = 89\,300$. It can be observed that higher Re values lead to larger particle transport, causing a higher particle accumulation at the center of the tank.

Further increases in Ro^{-1} or Re values lead to a larger radial inward transport of particles. However, depending on which parameter is varied (or if both are) and on the magnitude of the variation, the morphology of the particle bed changes in a different way. Examples of the patterns for different values of Re and Ro^{-1} are shown in Figs. 4–6. Figure 7 shows the position of the different types of patterns in the parameter space explored.

1. Increasing Re values

When only increasing the Re value and maintaining $\mathrm{Ro}^{-1} = 0$ (complete spin-down experiments), two typical patterns are observed, depending on the magnitude of Re. For $3 \times 10^4 \lesssim \mathrm{Re} \lesssim 5 \times 10^4$, particles are transported radially inward, causing the formation of complex spirals as seen in Fig. 4(b). This type of pattern is characterized by the elevation of the center of the particle bed ($r_{cr} = 0$), a number of deep spiral ripples surrounding it, and small areas near the tank wall with

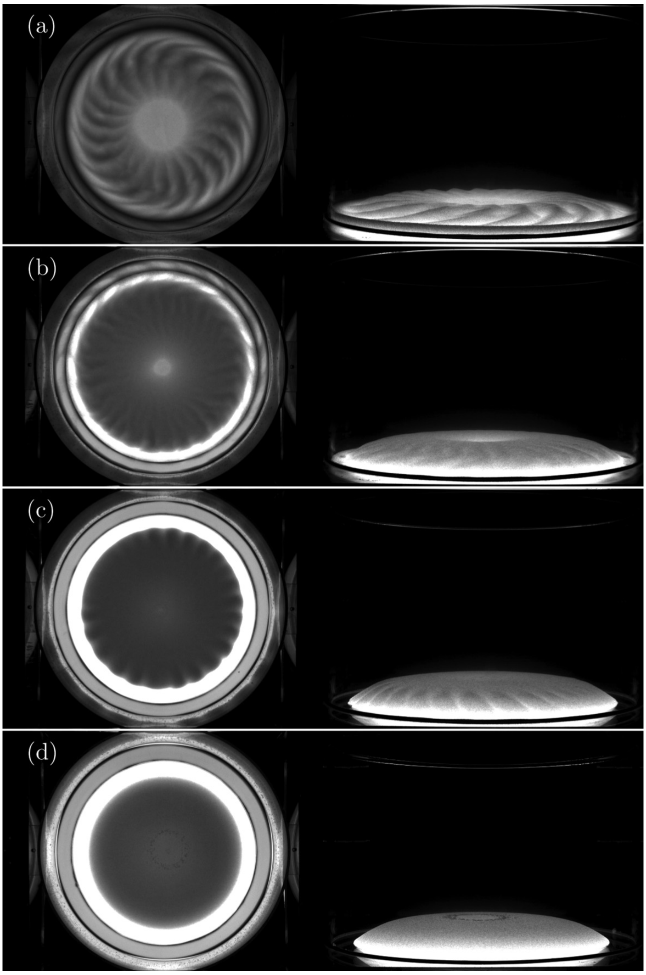

FIG. 5. Patterns formed in four experiments with $\mathrm{Ro}^{-1} > 1$ and $\mathrm{Re} = 17\,900$. (a) Crescent ripple pattern formed with $\mathrm{Ro}^{-1} = 2$. (b) Transition between a crescent ripple pattern and an annulus that occurred with $\mathrm{Ro}^{-1} = 3$. (c) Dome with ripples formed with $\mathrm{Ro}^{-1} = 4.3$. Spherical cap formed with $\mathrm{Ro}^{-1} = 7.6$. As the Ro^{-1} value increases, particle transport also increases, and smaller features (ripples) in the emerging patterns diminish.

no particles. In the case of the strongest flows ($\mathrm{Re} \gtrsim 5 \times 10^4$), an even larger amount of particles is transported radially inward, leaving areas devoid of particles and forming a pattern like the one in Fig. 4(c). Such patterns are characterized by a semiconical mound surrounded by spiral arms and by a lack of particles near the tank wall.

The formation of the patterns in strong complete spin-down experiments occurs as follows. For increasing Re values, the amount of particles transported radially inward increases, and particle motion becomes more turbulent, as seen in Fig. 8(a). Because of the inward motion, particles accumulate in the center of the tank (once $r_{cr} = 0$), elevating the central area to form a plateau [Fig. 8(b)]. During this convergence process, spiral arms develop due to the swirling motion, and the plateau increases in size as more particles continue to move radially inward (complex spirals emerge). The velocity at which particles converge at the center, the height at which the plateau is elevated, the length of the spiral arms, and if areas of the domain are left without particles depend on the Re value.

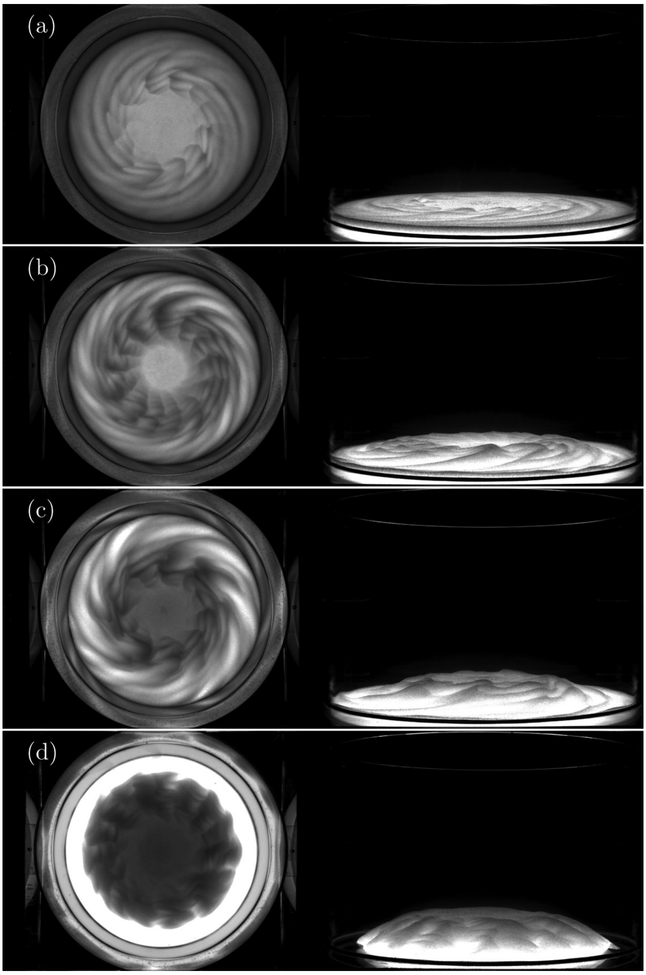

FIG. 6. Four examples of patterns observed for experiments with $\mathrm{Ro}^{-1} < 1$ (weak rotation) and different Re values. (a) Simple spiral pattern that emerged with $\mathrm{Re} = 23\,800$ and $\mathrm{Ro}^{-1} = 0.16$. (b) Transition between a crescent wave pattern and a simple spiral that emerged with $\mathrm{Re} = 23\,800$ and $\mathrm{Ro}^{-1} = 0.63$. (c) Complex spiral that emerged with $\mathrm{Re} = 29\,800$ and $\mathrm{Ro}^{-1} = 0.32$. (d) Dome with ripples that emerged with $\mathrm{Re} = 29\,800$ and $\mathrm{Ro}^{-1} = 0.8$.

In the case of high Re values, once the plateau forms, a portion of the particles is brought into suspension at approximately $R/2$. These particles continue spiralling toward the center of the tank, and with the rest of the (nonsuspended) particles, cause the plateau to be shaped into a semiconical mound. Once the hydrodynamic forces weaken, the mound recedes, particles settle, spiral arms become more defined around the plateau or mound formed, and features such as ripples develop. Both the length and number of the spiral arms decrease as the value of Re increases.

2. Increasing Ro^{-1} values

In cases where the Ro^{-1} value was varied while keeping Re constant (partial spin-down experiments), other types of patterns were observed. Taking as an example the experiments where Re was maintained at its lowest value ($\mathrm{Re} = 17\,900$) and Ro^{-1} was increased, three types of patterns emerged. Examples of these patterns are shown in Fig. 5. For weak background rotation

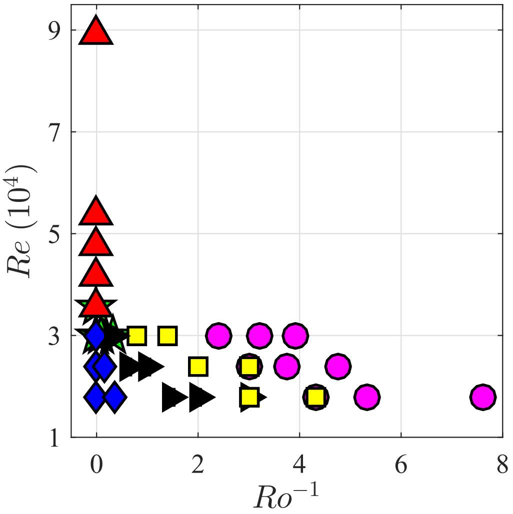

FIG. 7. Diagram of the parameter space explored showing the six different types of patterns. ◇ markers indicate the formation of spiral ripples. ▷ markers indicate the formation of crescent ripples. ⋆ markers indicate the formation of complex spirals. △ markers indicate the formation of a semiconical mound with spiral arms. ☐ markers indicate the formation of a dome with ripples along its contour. ○ markers indicate the formation of a spherical cap. Experiments with overlapping markers indicate that the emerging pattern shares characteristics of two typical patterns.

($0.5 \lesssim \mathrm{Ro}^{-1} \lesssim 2$), a pattern characterized by a sequence of symmetrical crescent ripples around the area where particles remain static forms [Fig. 5(a)]. At higher background rotation rates ($2 \lesssim \mathrm{Ro}^{-1} \lesssim 4$), a pattern like that in Fig. 5(c) emerges, consisting in a dome surrounded by ripples, and an area surrounding it is devoid of particles. As $\mathrm{Ro}^{-1} > 4$, the dome compresses and becomes smoother, forming a spherical cap, as seen in Fig. 5(d).

The formation of these patterns occurs as follows. For very low Ro^{-1} values ($0 \lesssim \mathrm{Ro}^{-1} \lesssim 0.5$), particles follow spiral trajectories and form simple spirals as those observed in weak complete spin-down experiments. As the Ro^{-1} value increases ($\mathrm{Ro}^{-1} \lesssim 0.5$), particles show an increased azimuthal motion and overall smoother particle movement. For example, for $\mathrm{Re} = 17\,900$ and $\mathrm{Ro}^{-1} \approx 1.5$, a larger swirling motion outside of the critical radius ($r > r_{cr}$) is observed, causing the initial spirals that emerge to be deformed into a sequence of symmetrical crescent ripples. The growth velocity of these crescent ripples increases with Ro^{-1}.

As Ro^{-1} continues to increase, the crescent ripples overlap and form a semitorus, as shown in Fig. 9(a). The inner region of this semitorus is characterized by the critical radius r_{cr}, and the outer region by an area devoid of particles. If the Ro^{-1} value is high enough, the internal diameter of the semitorus reduces until its collapse ($r_{cr} \to 0$), forming a particle dome, as shown in Figs. 9(b) and 9(c). The convergence velocity of the semitorus and the height of the dome depends on the value of Ro^{-1}. For the highest values of Ro^{-1} in this regime, we observed oscillations in the surface of the particle dome as it forms. As these oscillations decay, a very smooth spherical-cap dome forms.

Once the flow weakens, features, such as ripples, develop around the annulus or dome. These ripples become smaller as the Ro^{-1} value increases, completely vanishing for the experiments with the highest Ro^{-1} values.

Experiments with higher Re values ($\mathrm{Re} = 23\,800, 29\,800$) also show the formation of a dome by the collapse of a semitorus when $\mathrm{Ro}^{-1} \neq 0$. However, for $0.5 \lesssim \mathrm{Ro}^{-1} \lesssim 1$, particle motion is akin to what is observed in complete spin-down experiments (predominant spiralling motion). Furthermore, dome formation occurred at lower Ro^{-1} values due to the increased inward transport of particles.

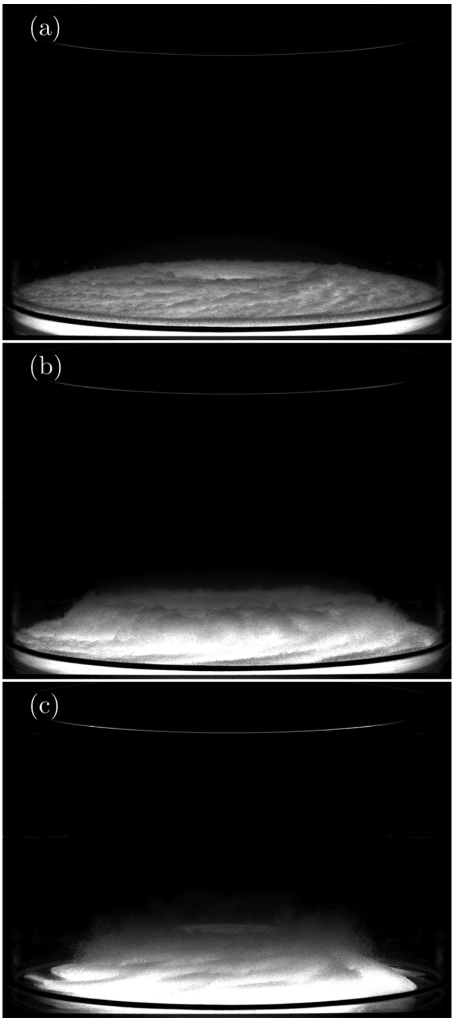

FIG. 8. Photographs showing the formation of a semiconical pattern. Images are taken from the experiment with $\Delta\Omega = 0.7\,\mathrm{rad\,s^{-1}}$ and $\Omega_f = 0$ ($\mathrm{Re} = 41\,700$, $\mathrm{Ro}^{-1} = 0$). The formation eventually collapses into a semiconical mound surrounded by spiral arms around it.

While ripples also emerge along the dome once the flow weakens, these are much rougher, in some cases forming folds as particles moved. Examples of experiments with $\mathrm{Re} = 23\,800$, 29 800, and two different values of Ro^{-1} each are shown in Fig. 6.

B. Net radial particle transport

For each experiment, Eq. (10) is used to calculate the local particle bed thickness $h_p(x, y, t)$. By subtracting the initial bed thickness $h_0 = h_p(x, y, t = 0)$ from h_p, the changes in bed thickness can be calculated

$$\Delta h(x, y, t) = h(x, y, t) - h_0. \tag{11}$$

An example of Δh is shown in Fig. 10 with its corresponding light intensity distribution I.

By separating the changes in bed thickness into its positive ($\Delta h^+ : \Delta h > 0$) and negative values ($\Delta h^- : \Delta h < 0$), the areas of deposition and erosion are identified. Integrating these values over the

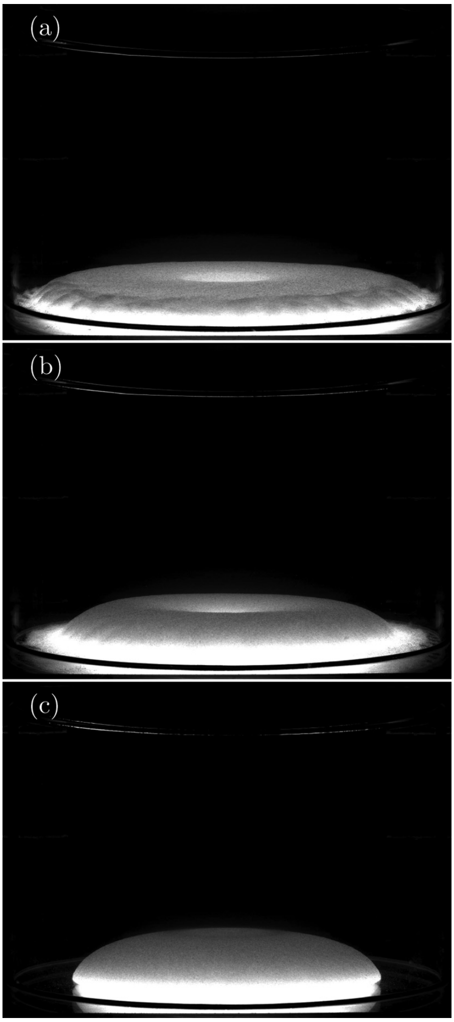

FIG. 9. Photographs showing the formation of a spherical-cap dome pattern. Images are taken from the experiment with $\Delta\Omega = 0.4\,\mathrm{rad\,s^{-1}}$ and $\Omega_f = 1.9\,\mathrm{rad\,s^{-1}}$ (Re $= 23\,800$, $\mathrm{Ro}^{-1} = 4.75$). Once the flow weakens, the dome flattens and small ripples emerge around it.

domain, we define the deposited (V_D) and eroded (V_E) particle volumes

$$V_D(t) = \iint\limits_A \Delta h^+ dA, \quad V_E(t) = \iint\limits_A \Delta h^- dA. \tag{12}$$

Since no particles are added or extracted during the experiments, the volume of particles eroded should equal the deposited particle volume. However, this condition is not exactly fulfilled due to measurement errors. To estimate the total error, the integral of Δh over the whole domain is used,

$$V_{\mathrm{Err}}(t) = \frac{(V_D + V_E)}{V_T} = \iint\limits_A \frac{\Delta h(x, y, t)}{h_0} dA, \tag{13}$$

where $V_T = \pi h_0 R^2$ is the volume of the flat particle bed at the beginning of the experiment. Since the light transmission through the particle bed decreases exponentially, the error is larger where the

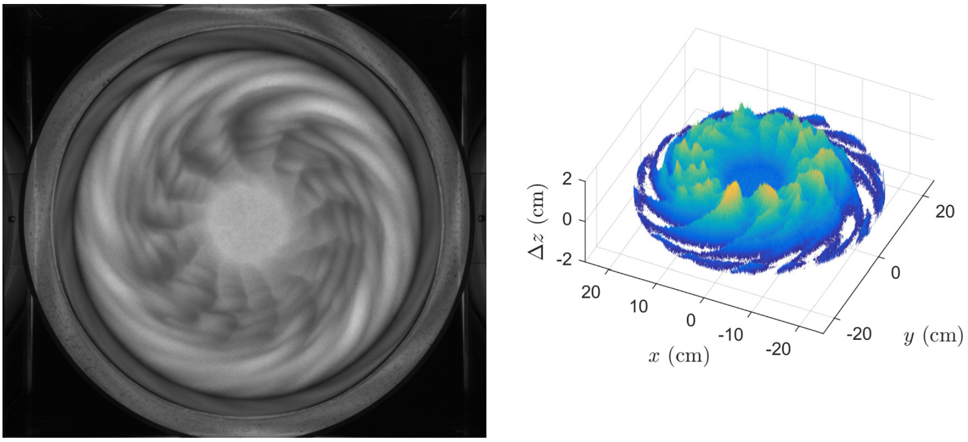

(a) (b)

FIG. 10. Example of a displacement field Δh (a) and its corresponding transmitted light intensity I recording (b). The experiment used in this example has parameter values of $\mathrm{Re} = 23\,800$ and $\mathrm{Ro}^{-1} = 0.625$.

bed is thicker. Therefore, we use the eroded particle volume V_E to compute the net radially displaced particle volume (V_{disp}).

Even though the magnitude of V_{disp} varies for each experiment, a similar overall behavior in time is observed, as shown for two experiments in Fig. 11. This common behavior is separated into three stages. First, there is an accumulation stage, where V_{disp} steadily increases due to the inward particle motion driven by the spin-down flow. Then, there is an equilibrium stage, where a nearly constant value of V_{disp} is reached since there is a balance between the hydrodynamic and gravity forces acting on the particles. This leads to the shape of the bed to remain static. Finally, there is a relaxation stage characterized by a decrease in V_{disp}. As the flow continues to decay, the hydrodynamic forces become weaker than gravity, pulling particles downslope. This stage is more

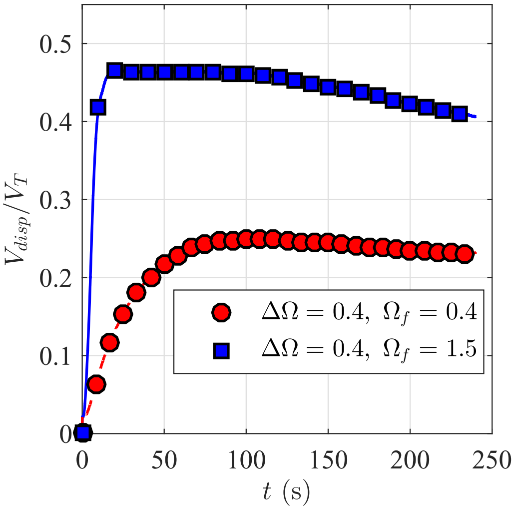

FIG. 11. Temporal behavior of the net displaced particle volume (V_{disp}) of two experiments with equal Re values but different Ro values. Circle markers indicate the experiment performed with $\mathrm{Re} = 23\,800$ and $\mathrm{Ro} = 1.0$. Square markers denote the experiment performed with $\mathrm{Re} = 23\,800$ and $\mathrm{Ro} = 0.27$.

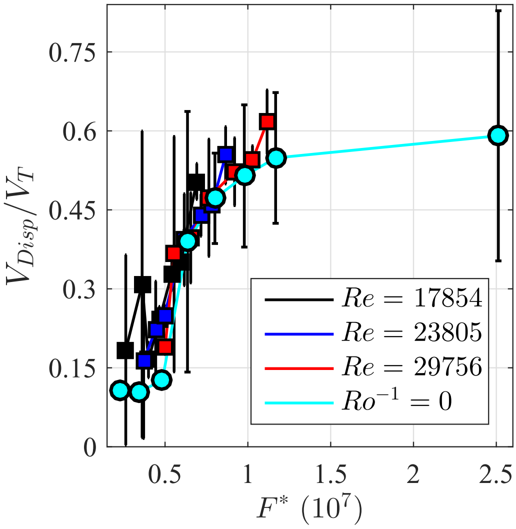

FIG. 12. Maximum net radially displaced particle volume (V_{disp}) as a function of the dimensionless total radial force exerted by the spin-down flow F^* [Eq. (7)]. Circle markers indicate complete spin-down experiments ($\text{Ro}^{-1} = 0$) and square markers partial spin-down experiments ($\text{Ro}^{-1} > 0$). Error bars indicate the difference between the total particle volume when the maximum V_{disp} occurs and the initial total particle volume V_T.

noticeable for high values of Re and Ro^{-1}, in which particles move downslope radially outward at the edge of the dome or steep semiconical mound when the flow weakens.

Further insight into the net radial particle transport is gained by comparing the maximum V_{disp} of each experiment with the total radial force F^* acting on the particle layer, defined in Eq. (7). Figure 12 shows the maximum V_{disp} as a function of F^*. Since F^* depends on both Re and Ro^{-1}, V_{disp} increases if either Re or Ro^{-1} increase. Weak flows (lowest values of Re and Ro^{-1}) displace a small amount of particles since the exerted shear stress is close to the critical shear stress ($\tau \sim \tau_{cr}$). Once the critical shear stress value is exceeded, there is an increase of particles that are displaced toward the center of the cylinder. This increase is similar for both the partial and complete spin-down experiments, even though there is a difference in magnitude in the value of Re.

As F^* approaches the largest values, V_{disp} reaches a saturation value. However, this behavior is not clear in cases where $\text{Ro}^{-1} > 0$. The saturation is caused by the occurrence of particle suspension, a limit in the packing of particles, and the angle of the dome formed in the center of the domain, where even in the cases of very high shear stress, particles cannot continue to be displaced radially inward.

While the error associated with the measurements of V_{disp} for large values of F^* is expected (mainly due to the occurrence of particle suspension), three experiments show a large error even for low values of F^*. It was found that the increase in the error is associated to the presence of finer particles (dirt, debris) which entered the tank due to the open top. In particular, in cases where background rotation is present ($\text{Ro}^{-1} > 0$), these finer particles are separated from the particle bed and transported radially inward where they accumulate. These particles can have a disproportionate effect on the transmitted light, adding to the measurement error, even if the volume fraction is negligible. Figure 13 shows a comparison between the estimated error in time for three experiments.

C. Minimal radius of a particle mound

Another relevant quantity related to the amount of sediment transport is the minimal radius of the sediment mound $R_{\min}$. This is obtained directly from the measurements, and in this section, we relate it to the total radial force to be able to predict the minimal extent of the particle mound. For

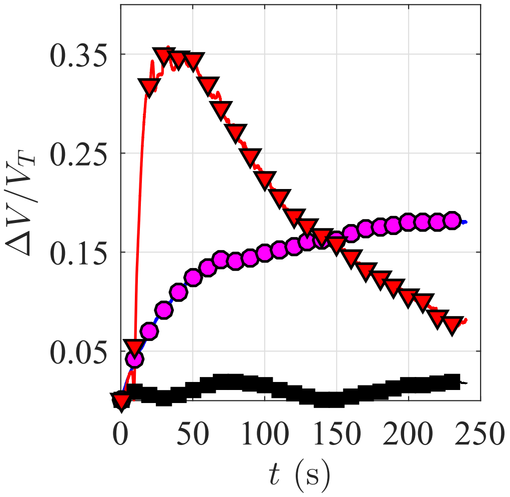

FIG. 13. Measurement of the error in time for three experiments. Each of them has a different cause of error. ▽ markers indicate the experiment where the largest amount of particle suspension occurred ($\mathrm{Re} = 89\,300$, $\mathrm{Ro}^{-1} = 0$). ○ markers indicate one of the experiments where small particles (debris) increased the error in the measurements ($\mathrm{Re} = 17\,900$, $\mathrm{Ro}^{-1} = 0.37$). □ markers indicate an experiment where particle suspension and small particle accumulation do not occur ($\mathrm{Re} = 23\,800$, $\mathrm{Ro}^{-1} = 1.0$).

this, we assume that the net radial force acting on a particle on the mound surface is zero (otherwise the radius of the mound would increase or decrease). This requires that the net gravitational force F_G (gravitational force minus the buoyancy force), the shear force exerted by the spin-down flow F_τ, and the net resistive force to motion (Coulomb force) F_c, be in balance:

$$\begin{gathered} F_\tau \cos\theta + F_c \cos\theta - F_g \sin\theta = 0, \\ F_\tau + \frac{4}{3}\mu_c \pi \rho_f g' \left(\frac{d}{2}\right)^3 - \frac{4}{3}\pi \rho_f g' \left(\frac{d}{2}\right)^3 \tan\theta = 0, \end{gathered} \tag{14}$$

where θ is the slope of the particle mound surface, μ is the Coulomb resistive parameter, $g' = (\rho_p/\rho_f - 1)g$ is the reduced gravity, g is the Earth's gravity, and d is the particle diameter.

Since the force applied by the flow on a particle F_τ is unknown, to solve Eq. (14) the force exerted over a single particle by the spin-down flow is considered to be proportional to the total radial force ($F_\tau = \alpha F_r$). To give an expression of the angle θ as a function of $R_{\min}$, the shape of the dome is approximated as a cone with a circular base, where the height of the dome h and its radius ($R_{\min}$) are related to the slope by $\tan\theta = h/R_{\min}$. Furthermore, since the volume of the dome $V_{cn} = \pi r^2 h/3$ is equal to the volume of the initial particle layer, the slope of the dome can be written as a function of only $R_{\min}$ [$\tan\theta = 3V_{cn}/(\pi {R_{\min}}^3)$]. Rewriting Eq. (14) with the previous relations, we obtain

$$\frac{2}{3}\alpha \pi \rho_f \nu^2 F^* + \frac{4}{3}\mu_c \pi \rho_f g' \left(\frac{d}{2}\right)^3 = \frac{4}{3}\pi \rho_f g' \left(\frac{d}{2}\right)^3 \frac{3V_{cn}}{\pi {R_{\min}}^3}, \tag{15}$$

which can be simplified to

$$\frac{1}{2}\frac{\alpha \nu^2}{g'(d/2)^3} F^* + \mu_c = \frac{3V_{cn}}{\pi {R_{\min}}^3}. \tag{16}$$

By plotting Eq. (16), as shown in Fig. 14, the values of both α and μ_c required for the equivalence to hold are calculated, yielding $\alpha = (1.477 \pm 0.100) \times 10^{-6}$ and $\mu_c = -0.013 \pm 0.034$. It was found that α approximately coincides with the ratio between the area of a single sediment particle and the

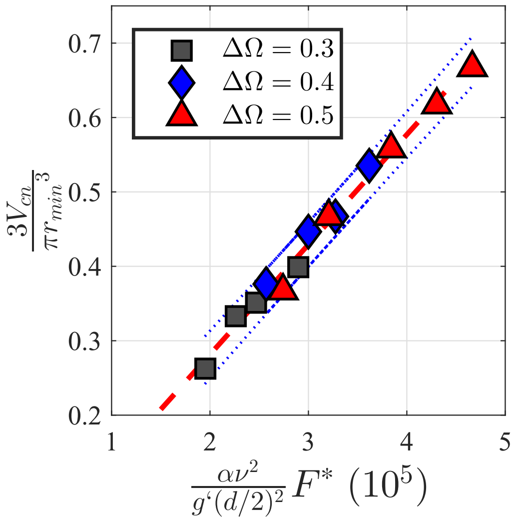

FIG. 14. Plot of the force balance presented in Eq. (16). Markers indicate the rotation difference in each experiment: $\Delta\Omega = 0.3\,\mathrm{rad\,s^{-1}}$ (□ markers), $0.4\,\mathrm{rad\,s^{-1}}$ (◇ markers), and $0.5\,\mathrm{rad\,s^{-1}}$ (△ markers). The fitted curve (dashed red line) follows $\alpha x + \mu = \Gamma$, where $\alpha = (1.477 \pm 0.100) \times 10^{-6}$, $\mu_c = -0.02 \pm 0.03$, $x = \nu^2/g'(d/2)^3 F^*$, and $\Gamma = 3V_{cn}/(\pi R_{\mathrm{min}}^3)$. The prediction bounds are indicated by the dotted blue line.

area of the bottom of the tank $(d/2)^2/R^2 = 1.4126 \times 10^{-6}$. As for μ_c, due to its very small value, it is understood that F_c plays a negligible role in the force balance.

Furthermore, by isolating R_{min} and leaving as a function of Re and Ro, we obtain

$$R_{\mathrm{min}} = \left\{ \frac{3V_{cn}}{\pi\left[\frac{1}{2}\frac{\alpha\nu^2}{g'(d/2)^3}\tau^*\mathrm{Re}^{3/2}\sqrt{1+\mathrm{Ro}^{-1}} + \mu_c\right]} \right\}^{1/3}. \tag{17}$$

From this equation and Fig. 15, it can be seen that the minimal radius a particle dome can achieve is inversely proportional to ${F^*}^{1/3} = \tau^*\mathrm{Re}^{3/2}\sqrt{1+\mathrm{Ro}^{-1}}^{1/3}$.

The experiments used to validate this approximation are limited to those with $\mathrm{Ro}^{-1} \geqslant 1$ because more symmetric dome formations occur and particle suspension is low. This is of extreme importance, as the occurrence of particle suspension means that the volume of particles is not conserved.

D. Particle suspension

Particles are brought into suspension by the flow in certain experiments, shown in Fig. 16. Small or no final rotation (small or null Ro^{-1} values) and relatively strong flows (medium to high Re values) are required for particle suspension to occur. The amount of particle suspension increases for higher Re values (complete spin-down experiments having the largest particle suspension) and decreases for higher values of Ro^{-1}.

To determine the cause of the particle suspension, a vertical laser sheet was used to illuminate the tank from the side and tracer particles were added to the fluid. This allowed us to observe the generation of turbulence at the side wall caused by centrifugal instabilities originating from the differential rotation due to the no-slip condition [37–43]. The turbulence is then advected toward the interior of the cylinder due to the secondary motion, causing particle suspension. An image taken with the side camera revealing the presence of the wall turbulence generated in the tank is shown in Fig. 17. Unfortunately, no quantitative measurements could be made about the amount of

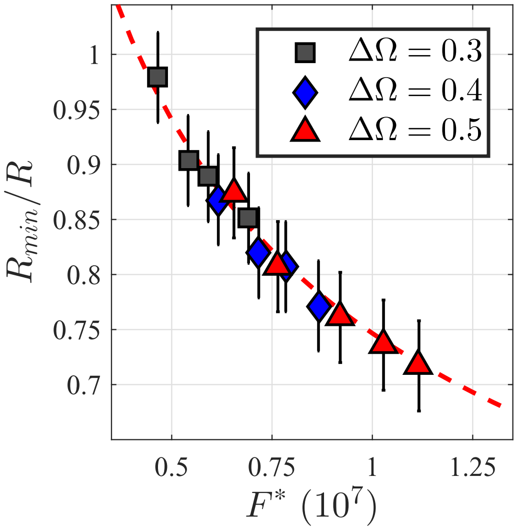

FIG. 15. Minimal radius of a particle mound for the partial spin-down experiments as a function of the dimensionless force F^* [Eq. (7)]. The marker's shape indicate the same experiments as in Fig. 14. Error bars indicate the standard deviation in the measured sediment bed radius. The fitted curve (dashed red line) follows Eq. (17), where $\mu = 0$.

particle suspension due to the suspended particles quickly traveling into and out of the illuminated volume of the laser sheet.

Although different magnitudes of the vertical velocity of the secondary motion were achieved with different Re values, particles were not suspended (or lifted) because of this mechanism. Turbulence appears to be the primary cause of particle suspension. However, it was observed that

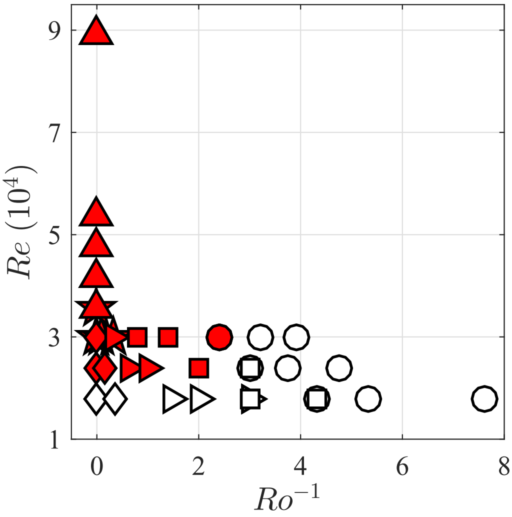

FIG. 16. Diagram of the explored parameter space showing the experiments where particles were suspended or not. Filled symbols are experiments for which particle suspension occurred during spin-down. Experiments denoted with empty symbols showed no particle suspension. The marker's shape indicate the same regimes as in Fig. 7.

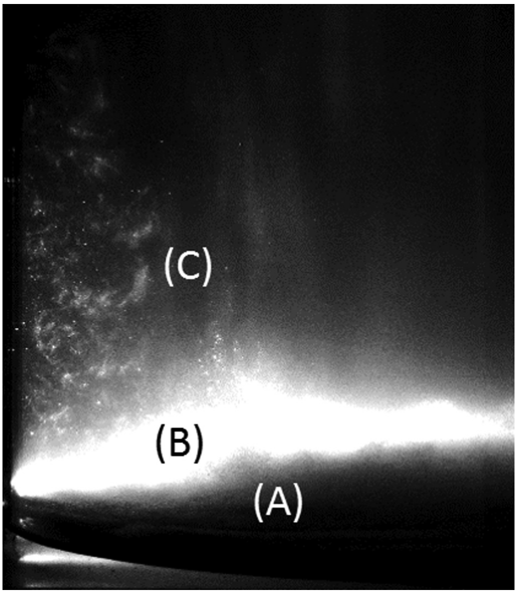

FIG. 17. Side view of the particle layer illuminated by a vertical laser sheet for an experiment $\Delta\Omega = 0.6\,\text{rad}\,\text{s}^{-1}$ and $\Omega_f = 0\,\text{rad}\,\text{s}^{-1}$ ($\text{Re} = 35700$, $\text{Ro}^{-1} = 0$). The side camera is placed at a shallow angle for an oblique view. Only half of the tank is shown, with the side wall located on the left of the image. A mix of sediment particles and tracer particles is used to visualize the flow. Three distinct regions are observed: (A) the surface of the particle bed that is not completely illuminated, (B) sediment particles illuminated by the vertical laser sheet, and (C) tracer particles illuminated by the laser. In region (C) isolated patches of high particle concentration can be observed, indicating the presence of turbulent structures. These structures are only observed for the experiments with a low Ro^{-1} value.

the shape of the dome can lead to particle deflection, causing additional particle suspension. In such cases, the suspension caused by this effect is much less than that produced by turbulence, and since the roughness and asymmetric features (such as spiral arms) decrease with higher Ro^{-1} values, the particle suspension due to this mechanism also diminishes.

V. DISCUSSION

The observed differences in the bed patterns reveal that both inertial and rotation effects (characterized by Re and Ro) govern the flows dynamics, and hence, the bed evolution. In particular, rotation is observed to play a mayor role in the trajectory of particles, the regularity of the bed patterns, and the occurrence of particle suspension.

Although particles follow a spiral trajectory regardless of the type of spin-down flow generated, changes in the curvature of the trajectory are observed when background rotation is present ($\text{Ro}^{-1} > 0$). This can be explained by following the calculation of Schlichting *et al.* [15] of the dimensionless radial and azimuthal shear stress values for the Ekman and Bödewadt-type flows. Here, it is found that the relative magnitude of the azimuthal shear stress increases as it approaches an Ekman-type flow. Therefore, it is understood that as Ro^{-1} increases, so will the curvature of the spiral trajectory that particles follow. This can be observed in Figs. 8 and 9, where the change in the curvature of the spiral motion causes particles to accumulate in a different way, leading to the formation of a plateau or a toroid.

A further effect due to background rotation ($\text{Ro}^{-1} > 0$) is the suppression of three-dimensional motions (following the Taylor-Proudman theory). This leads to less turbulent particle motion, thus lowering the occurrence of particle suspension as Ro^{-1} increases, causing the emergence of smooth particle domes for experiments with high Ro^{-1} values. In contrast, experiments with $\mathrm{Ro}^{-1} = 0$ show significant particle suspension and motion is observed to be more turbulent, leading to the formation of patterns composed of a number of spirals with small features (such as ripples). These patterns are reminiscent of previous experiments performed in granular beds [28–30], where it is discussed that type I and type II instabilities (as described by Faller [44] and by Savas [40]) play a role in the formation of patterns. This is also consistent with the lack of smaller features as the Ro^{-1} value increases since instabilities are suppressed with the presence of background rotation.

The results show that the net particle displacement can be explained by the total radial force F_r exerted by the boundary layer on the sediment. Even if this radial force is computed for a laminar, unbounded case, the curves plotted in Fig. 12 collapse, indicating that the formation of patterns and the role of the side walls are secondary in determining the net transport. The role of side walls has previously been shown to be of secondary importance in the dynamics and evolution of spin-down flows [16,43], particularly at timescales much shorter than the typical decay time, as in our experiments. However, we did observe the side walls to have an impact in the generation of turbulence and the suspension of sediment. This is due to the no-slip condition at the side wall, where a differential rotation is induced, leading to centrifugal forces that cause instabilities in the flow [37–42].

While a single type of particles was used in this study, the presence of lighter and smaller particles (debris) inside the experimental setup for three experiments allowed us to gain insight into the transport of lighter particles (but still heavier than the fluid). These smaller particles are transported radially inward before the larger particles and concentrate in the center of the tank even for low values of F^*. From this, it is possible to use a spin-down flow to separate different particle types based on the τ_{cr} value required to move them. However, depending on the parameter values, the accumulation of smaller particles formed can remain relatively intact ($\mathrm{Ro}^{-1} > 1$) or be mixed throughout the domain due to turbulence ($\mathrm{Ro}^{-1} = 0$). In the case of heavier particles, Refs. [28–30] use denser particles to compose the sediment bed ($1.8\,\mathrm{g\,cm^{-3}} < \rho_p < 7.9\,\mathrm{g\,cm^{-3}}$; $55\mu\mathrm{m} < r_p < 1585\mu\mathrm{m}$) and also observe (spiral) patterns, even at higher Re and Ro values than those used in the present study. This indicates that sediment beds consisting of other types of particles (or mixtures of) can also develop similar patterns.

Clearly, the response of the bed to the flow depends on the particle properties. While particle size, density, and shape might affect the patterns formed, we expect that particle transport will occur as in this study as long as the transport remains as bed load.

VI. CONCLUSION

With the use of a simple experimental setup, we describe the effect of representative boundary layers under a swirling flow over a particle layer in a cylindrical domain. In particular, we describe the emergence and formation of patterns in the sediment bed, the net radial transport, and the occurrence of particle suspension. For a given sediment type, both the intensity of the flow (given by the Re value) and the intensity of background rotation (represented by the Ro value) govern both the type of generated spin-down flow and the morphodynamics of the sediment bed. In the $(\mathrm{Re}, \mathrm{Ro}^{-1})$ parameter space explored, six characteristic patterns were found.

By redefining the boundary layer thickness δ of the spin-down flow, a dimensionless force (valid for both partial and complete spin-down experiments) is defined as $F^* = \tau^*\mathrm{Re}^{3/2}\sqrt{(1 + \mathrm{Ro}^{-1})}$. Although F^* is obtained through a simple model of a laminar, stationary boundary layer without lateral boundaries, there is a good collapse of the measured maximum net radial transport, as seen in Fig. 12. This indicates that the total radial applied force is the primary cause of the radial displacement of particles. Additionally, quantitative predictions about R_{min} can be made by performing a balance between the gravity force and F^* if particle suspension is limited.

The force F^* can be increased either by increasing the table's deceleration (increasing the value of Re) or increasing the rotation rate (increasing the value of Ro^{-1}). In terms of the dynamics, these two options are very different. Increasing Re values generates instabilities and subsequently turbulence. On the other hand, increasing Ro values suppresses instabilities and three-dimensional motions. In general, our experiments show a very different evolution for experiments with large Re values and $\mathrm{Ro}^{-1} = 0$, when compared with experiments with increasing Ro values and relatively small Re values (e.g., $\mathrm{Re} = 17\,900$ or $23\,800$).

It is then of particular interest that, in spite of these differences, measurements of the net radially displaced particle volume (V_{disp}) depend exclusively on F^*. This indicates that background rotation leads to flows that are more efficient in transporting sediment to the center of the domain. This is due to a decrease in the boundary layer thickness and hence an increase in the bottom shear stress. It is then concluded that the differences in the stability of the Bödewadt and Ekman boundary layers are observed in the patterns that form. However, the similarity in the structure of these boundary layers (including intermediate cases) is observed in their capability to transport sediment to the core of swirling flows.

ACKNOWLEDGMENTS

This study was financially supported by CONACYT (Mexico) through a scholarship grant for A.S.G.V. (Grant No. 383903) and by the NWO/VENI (The Netherlands) grant to M.D.M. (Grant No. 863.13.022).

[1] S. S. Tigner, Empedocles' twirled ladle and the vortex-supported Earth, Isis **65**, 433 (1974).

[2] J. T. Snow, On the formation of particle sheaths in columnar vortices, J. Atmos. Sci. **41**, 2477 (1984).

[3] R. Greeley, M. R. Balme, J. D. Iversen, S. Metzger, R. Mickelson, J. Phoreman, and B. White, Martian dust devils: Laboratory simulations of particle threshold, J. Geophys. Res. Planets **108**, 5041 (2003).

[4] D. O. Cook, The occurrence and geologic work of rip currents off southern California, Mar. Geol. **9**, 173 (1970).

[5] J. H. MacMahan, E. B. Thornton, and A. J. H. M. Reniers, Rip current review, Coast. Eng. **53**, 191 (2006).

[6] D. W. Pepper, *Dispersion of Small Particles in a Tornado* (EI du Pont de Nemours, Aiken, 1975).

[7] M. A. Magsig and J. T. Snow, Long-distance debris transport by tornadic thunderstorms. Part I: The 7 May 1995 supercell thunderstorm, Mon. Weather Rev. **126**, 1430 (1998).

[8] D. C. Lewellen, B. Gong, and W. S. Lewellen, Effects of finescale debris on near-surface tornado dynamics, J. Atmos. Sci. **65**, 3247 (2008).

[9] G. R. Gust, Fluid velocity measurement instrument, US Patent No. 4,986,122 (January 22, 1991).

[10] S. V. Apte, K. Mahesh, P. Moin, and J. C. Oefelein, Large-eddy simulation of swirling particle-laden flows in a coaxial-jet combustor, Int. J. Multiphase Flow **29**, 1311 (2003).

[11] Z. Chen, Z. Li, J. Jing, L. Chen, S. Wu, and Y. Yao, Gas/particle flow characteristics of two swirl burners, Energ. Convers. Manage. **50**, 1180 (2009).

[12] M. Jakubowski, Secondary flows occurring in a whirlpool separator – A study of phenomena – observation, simulation and measurements, Chem. Process Eng. **36**, 277 (2015).

[13] A. Einstein, The cause of the formation of meanders in the courses of rivers and of the so-called Baer's law, Naturwissenschaften **14**, 223 (1926).

[14] E. R. Benton and A. Clark Jr., Spin-up, Annu. Rev. Fluid Mech. **6**, 257 (1974).

[15] H. Schlichting and K. Gersten, *Boundary-Layer Theory* (Springer, Berlin, 2017).

[16] H. P. Greenspan and L. N. Howard, On a time-dependent motion of a rotating fluid, J. Fluid Mech. **17**, 385 (1963).

[17] G. K. Batchelor, Note on a class of solutions of the Navier-Stokes equations representing steady rotationally symmetric flow, Q. J. Mech. Appl. Math. **4**, 29 (1951).

[18] T. von Kármán, Über laminare und turbulente reibung, Z. Angew. Math. Mech. **1**, 233 (1921).

[19] U. T. Bödewadt, Rotary currents on fixed grounds, Z. Angew. Math. Mech. **20**, 241 (1940).

[20] M. H. Rogers and G. N. Lance, The rotationally symmetric flow of a viscous fluid in the presence of an infinite rotating disk, J. Fluid Mech. **7**, 617 (1960).

[21] E. H. Wedemeyer, The unsteady flow within a spinning cylinder, J. Fluid Mech. **20**, 383 (1964).

[22] E. Crespo del Arco, E. Serre, P. Bontoux, and B. E. Launder, Stability, transition, and turbulence in rotating cavities, in *Instability of Flows*, Vol. 6, edited by M. Rahman (WIT, Southampton, 2005), pp. 141–195.

[23] J. P. Johnston, Effects of system rotation on turbulence structure: A review relevant to turbomachinery flows, Int. J. Rotating Mach. **4**, 97 (1998).

[24] J. Pedlosky, The spin up of a stratified fluid, J. Fluid Mech. **28**, 463 (1967).

[25] R. C. Beardsley, A laboratory model of the wind-driven ocean circulation, J. Fluid Mech. **38**, 255 (1969).

[26] A. Eliassen, On the Ekman layer in a circular vortex, J. Meteorol. Soc. Jpn. **49**, 784 (1971).

[27] A. E. Hill, Spin-down and the dynamics of dense pool gyres in shallow seas, J. Mar. Res. **54**, 471 (1996).

[28] P. J. Thomas, Pattern formation of granules on the bottom of a differentially rotating tank, J. Fluid Mech. **274**, 23 (1994).

[29] P. J. Thomas and F. Zoueshtiagh, Rotating-disk-type flow over loose boundaries, J. Eng. Math. **57**, 317 (2007).

[30] H. Caps and N. Vandewalle, Granular spirals on erodible sand bed submitted to a circular fluid motion, Phys. Rev. E **68**, 031303 (2003).

[31] R. J. Munro and S. B. Dalziel, Attenuation technique for measuring sediment displacement levels, Exp. Fluids **39**, 602 (2005).

[32] G. K. Batchelor, *An Introduction to Fluid Dynamics* (Cambridge University Press, Cambridge, UK, 1967).

[33] R. J. Lingwood, Absolute instability of the Ekman layer and related rotating flows, J. Fluid Mech. **331**, 405 (1997).

[34] C. A. Fleming and J. N. Hunt, Application of sediment transport model, in *Coastal Engineering 1976* (ASCE, New York, 1977), pp. 1184–1202.

[35] D. Paphitis, Sediment movement under unidirectional flows: An assessment of empirical threshold curves, Coast. Eng. **43**, 227 (2001).

[36] J. P. Le Roux, Grains in motion: A review, Sediment. Geol. **178**, 285 (2005).

[37] H. Görtler, On the three-dimensional instability of laminar boundary layers on concave walls, NACA-TM-1375, 1954.

[38] F. Bien and S. S. Penner, Spin-up and spin-down of rotating flows in finite cylindrical containers, Phys. Fluids **14**, 1305 (1971).

[39] G. P. Neitzel and S. H. Davis, Centrifugal instabilities during spin-down to rest in finite cylinders. numerical experiments, J. Fluid Mech. **102**, 329 (1981).

[40] Ö. Savas, Stability of Bödewadt flow, J. Fluid Mech. **183**, 77 (1987).

[41] V. Denk and A. Dürholt, Experimental investigations of the unsteady rotating flow field in a cylindrical vessel, Exp. Fluids **12**, 97 (1991).

[42] G. Gauthier, P. Gondret, and M. Rabaud, Axisymmetric propagating vortices in the flow between a stationary and a rotating disk enclosed by a cylinder, J. Fluid Mech. **386**, 105 (1999).

[43] P. D. Weidman, On the spin-up and spin-down of a rotating fluid. Part 2. Measurements and stability, J. Fluid Mech. **77**, 709 (1976).

[44] A. J. Faller, An experimental study of the instability of the laminar Ekman boundary layer, J. Fluid Mech. **15**, 560 (1963).